



# Thermoelectric performance of cadmium-based LiCdX (X = N, P, As, Sb and Bi)-filled tetrahedral semiconductors: applications in green energy resources

PALLAVI<sup>1</sup>, CHANDRAVIR SINGH<sup>1</sup>, PEEYUSH KUMAR KAMLESH<sup>2</sup>, RAJEEV GUPTA<sup>3</sup>  
and AJAY SINGH VERMA<sup>4</sup> \*

<sup>1</sup>Department of Physics, Agra College, Agra 282 002, India

<sup>2</sup>School of Basic and Applied Sciences, Nirwan University Jaipur, Rajasthan 303 305, India

<sup>3</sup>Department of Physics, School of Engineering, University of Petroleum and Energy Studies, Dehradun, Uttarakhand 248 007, India

<sup>4</sup>Division of Research & Innovation, School of Applied and Life Sciences, Uttaranchal University, Dehradun, Uttarakhand 248 007, India

\*Corresponding author. E-mail: [ajay\\_phy@rediffmail.com](mailto:ajay_phy@rediffmail.com)

MS received 1 November 2022; revised 24 April 2023; accepted 9 May 2023

**Abstract.** Half-Heusler materials have been studied on a large scale due to their high stability and wide range of band gaps. Here, we have studied the fundamental physical and thermoelectric parameters of LiCdX (X = N, P, As, Sb and Bi) and observed that these compounds have F43m space group with 5.31, 6.06, 6.25, 6.64 and 6.81 Å lattice constants for LiCdN, LiCdP, LiCdAs, LiCdSb and LiCdBi, respectively. All compounds exhibit direct band-gap semiconducting behaviour except LiCdBi which shows a metallic nature. In near-infrared and visible regions, these compounds show excellent photovoltaic behaviour, but they restrict far-infrared and ultraviolet radiation. By examining thermoelectric characteristics, we have analysed that at 300 K, ZT achieves unity in both the *p*- and *n*-regions for three of these materials, making them prospective thermoelectric candidates at ambient temperature. The studied thermodynamic properties have confirmed that materials are stable which will motivate experimentalists.

**Keywords.** Half-Heusler; refractive index; seebeck coefficient; absorption coefficient; figure of merit.

**PACS Nos** 62.20.Dc; 71.15.Nc; 77.22.Ch; 78.20.Ci

## 1. Introduction

Photovoltaics and thermoelectric generators play vital roles in fulfilling the requirement of energy, that too without greenhouse gas emissions. For these applications, among a large variety of materials, half-Heusler materials (space group F43m, 216) are the most investigated materials. There are many distinct types of materials in this category, each with unique physical characteristics and uses. Among the functional materials based on these compounds are topological insulators, piezoelectric semiconductors, thermoelectric semiconductors and optoelectronic semiconductors [1–4]. Some binary semiconductors have a narrow range of uses. Half-Heusler compounds with the chemical formula XYZ, also known as “Nowotny-Juza”, however, belong to a unique class of materials [5]. Numerous semiconductors with large band gaps belong to the eight-electron

half-Heusler class [6]. A few *ab-initio* calculations [7–14] have been conducted to date on potential half-Heusler materials with eight electrons (I–II–V and I–III–IV types).

Recently, Rani *et al* [15] studied various physical parameters of the PdVGa half-Heusler compound and suggested it as a direct band-gap semiconducting material, which is suitable for optoelectronic applications. Casper *et al* [16] thoroughly reviewed half-Heusler compounds and mentioned that these materials can serve potentially in spintronics, topological insulators, thermoelectric, solar cells, etc. Khandy *et al* [17] theoretically studied various physical parameters and stability criteria of PtXSn (X = Zr, Hf) semiconductor materials and suggested them as potential materials for thermoelectric generators having a large figure of merit. Bouafia *et al* [18] have done a stability and structural analysis of LuAuSn half-Heusler material. They

also studied the bonding and interactions of its atoms. Its vibrational analysis confirmed that it is dynamically stable in its ground state, indicating that even at very low temperatures its structure remains the same. Ye *et al* [19] investigated the thermoelectric performance of PCdNa half-Heusler compound and reported that it has an unusually low thermal conductivity and suggested that PCdNa is a promising p-type high-temperature half-Heusler thermoelectric material with a figure of merit  $ZT = 3.3$  at 900 K for optimum p-type doping. Sarwan *et al* [20] observed LiZnP and LiCdP as direct band-gap materials and their fascinating thermodynamic properties open a wide scope of their technological applications. Yadav and Sanyal [21] investigated Li- and Cd-based half-Heusler alloys and found them to exhibit a high power factor for p-type doping. Mellouki *et al* [22] computed structural and elastic properties of LiCdX ( $X = \text{N, P, As}$ ) half-Heusler compounds and found them mechanically stable.

This study used density functional theory (DFT) to investigate the half-Heusler materials LiCdX ( $X = \text{N, P, As, Sb and Bi}$ ). Because of their significance in optoelectronic and thermoelectric devices, these materials, which are Nowotny–Juza filled-tetrahedral structures, have been the focus of several experimental and theoretical research [23]. Most of these materials have previously been investigated to compute their structural, elastic, vibrational, electronic and optical properties within the context of DFT, employing the generalised gradient approximation (GGA) and local density approximation (LDA) exchange–correlation potentials, which are recognised for drastically underestimating the band gap of the semiconductor and insulator materials [22–25].

To understand and predict some of the material's characteristics and technological applicability, it is important to determine the electronic structure of the material precisely. This fact motivated the study of structural, optoelectronic, thermoelectric and dynamic parameters of LiCdX ( $X = \text{N, P, As, Sb and Bi}$ ) ternary substances using highly precise approximations to the exchange–correlation potential, which is the first aim of the current work. Also, until now including the electronic and optical properties of LiCdBi, the dynamic and thermoelectric parameters of the titled materials have not been investigated thoroughly. Consequently, the second aim of this work is to predict the fundamental properties of these compounds. Hence, this work aims to give a detailed description of the fundamental physical and thermoelectric investigations of LiCdX ( $X = \text{N, P, As, Sb and Bi}$ ) materials by using the first-principles study.

## 2. Computational details

We used the full-potential linearised augmented plane wave (FP-LAPW) approach in the WIEN2k simulation code for a majority of the parameters. Generalised gradient approximation (GGA) with Wu–Cohen (WC) [26] and Perdew–Burke–Ernzerhof (PBE) [27] configurations have been utilised as the exchange–correlation functional to study the lattice parameters and optimise the crystal structure, while to study the rest of the parameters PBE-GGA exchange potential with Tran and Blaha modified Becke and Johnson approach (TB-mBJ) [28] has been used. In LiCdX ( $X = \text{N, P, As, Sb and Bi}$ ), the muffin-tin radii for Li were taken as 1.90, 2.22, 2.05, 2.12, and 2.11 atomic unit (a.u.) respectively; for Cd were taken as 2.26, 2.50, 2.48, 2.50, and 2.50 a.u. respectively; for X-atom were taken as 1.85, 2.05, 2.35, 2.50, and 2.50 a.u. respectively. We have taken  $-6$  eV cut-off energy to ensure no charge leakage from the core states and have taken  $10 \times 10 \times 10$  k-points in the first Brillouin zone for investigating structural parameters, while for all other parameters,  $50 \times 50 \times 50$  k-points have been used. The SCF cycles converged for total energy and charge variation in sequential iterations were less than  $10^{-5}$  Ry and  $10^{-4}$  units correspondingly.

## 3. Results and discussion

### 3.1 Structural information

Half-Heusler compounds (LiCdX) form in the space group F43m (no.-216) with atoms Li, Cd, and X at 4b(0.5,0.5,0.5), 4a(0,0,0) and 4c(0.25,0.25,0.25) Wyck-off sites, respectively. Employing Birch–Murnaghan equation of state (EOS) [29,30], lattice constant  $a$  (in Å) at equilibrium state, bulk modulus  $B$  (in GPa) at zero pressure and first pressure derivative of the bulk modulus ( $B'$ ) have been calculated.

Table 1 shows that the lattice constants and other structural parameters calculated by WC-GGA are in best agreement with the previously calculated parameters. Figure 1 exhibits the energy–volume relationship of these materials. The volume of a unit cell of the particular material corresponding to the minimum energy provides the most stable structure of the material, from which we can measure the lattice constant at the equilibrium state. We have perceived that lattice constant ( $a$ ) of LiCdX is between 5.31 and 6.81 Å and it shows increment with an increasing atomic number of X atoms; which holds good with the theoretical notion. The bulk modulus at zero pressure follows the inverse correlation as the lattice constants of these materials as shown in table 1. As the X-atom's atomic number rises, so

**Table 1.** Structural, electronic and optical parameters of LiCdX (X = N, P, As, Sb and Bi) half-Heusler compounds.

Compounds	$a$ (Å)			$B$ (GPa)			Band gap (eV)				
	WC	PBE	Other	WC	PBE	Other	PBE	PBE + mBJ	Dielectric constant $\epsilon_1(0)$	Refractive index $n(0)$	Reflectivity $R(0)$
LiCdN	5.31	5.38	5.30 <sup>b</sup>	98.81	87.8	–	0	0.33, 0.32 <sup>b</sup>	7.27, 7.52 <sup>b</sup>	2.697, 2.742 <sup>b</sup>	0.211
LiCdP	6.06	6.14	6.05 <sup>b</sup> , 6.09 <sup>d*</sup>	60.89	54.6	–	0.69	1.60, 1.3 <sup>e*</sup> , 1.65 <sup>b</sup>	7.90, 7.88 <sup>b</sup>	2.812, 2.808 <sup>b</sup>	0.226
LiCdAs	6.25	6.34	6.26 <sup>a*</sup> , 6.24 <sup>b</sup>	53.34	47.3	58.9 <sup>c</sup>	0	0.93, 0.96 <sup>b</sup>	9.33, 9.32 <sup>b</sup> , 15.46 <sup>c</sup>	3.056, 3.053 <sup>b</sup> , 3.932 <sup>c</sup>	0.257
LiCdSb	6.64	6.74	6.63 <sup>b</sup>	43.45	37.2	–	0.35	1.07, 1.1 <sup>b</sup>	11.03, 10.93 <sup>b</sup>	3.322, 3.307 <sup>b</sup>	0.289
LiCdBi	6.81	6.93	–	37.74	32.5	–	0	0	19.18	4.383	0.395

\*Signifies experimental study

<sup>a</sup>Ref. [49], <sup>b</sup>ref. [23], <sup>c</sup>ref. [50], <sup>d</sup>ref. [6] and <sup>e</sup>ref. [51]

does the bulk modulus of the compounds. As a result, we understood that the heavier the material, the more compressible it is. The fact that the lattice parameters are varying confirms the study's accuracy and reliability.

### 3.2 Electronic properties

The electronic band structure affects the precision of the further investigated parameters. The band structure has been explained, and various optical and thermoelectric parameters have been analysed. The first Brillouin zone's band structure plots between the energy function and wave vector  $k$  are shown in figure 2. These graphs show that except LiCdBi all other materials are direct band-gap semiconductors, whereas LiCdBi shows metallic nature. The directivity of the band gap of these materials is at  $\Gamma$ -point. The calculated band gaps of LiCdX (X = N, P, As, Sb and Bi) half-Heusler materials using PBE and PBE + mBJ potential functionals are listed in table 1. To learn more about the makeup of these compounds' band structure, we determined the density of states (DOS). The partial and total density of states (PDOS and TDOS) of these specimens for the equilibrium lattice constant have been computed with PBE + mBJ formulation of potential functionals and showcased in figure 3. By analysing PDOS and TDOS graphs with the band structure, a decent correlation is detected.

TDOS can be described by splitting its graph into three regions – two regions are dedicated to the valance band (lower and upper), while one region is dedicated to the conduction band. The electronic distribution in LiCdN and LiCdAs is dissimilar from that of the other studied materials in the lower valance band section (–5 to –3 eV), according to DOS analysis. In this region, in LiCdN and LiCdAs major electronic contribution comes from the X's  $p$ -orbital, and minimal involvement comes from the  $s$ -orbital of Cd, whereas in all other materials, it is  $s$ - $p$  hybridisation of Cd and X atom, respectively. In the upper valance band section (–3 to 0 eV) of all the studied materials, major electronic involvement appears from the  $p$ -orbital of X and very less involvement (except LiCdN) comes from the  $s$ -orbital of Cd while in LiCdN the minor involvement is from the  $d$ -orbital of Cd. In both the regions (lower and upper) of the valance band of all the compounds, the involvement of the Li atom is very small. In the third region (conduction band), near the minima of all the compounds of our interest (except LiCdN) the dominant electronic states come from the  $s$ -orbital of Cd with lesser involvement of the  $p$ -orbital of X, whereas in LiCdN it is vice-versa. In this region also, the involvement of the Li atom is quite negligible. In the comparison between figures 3a and 3b, it has been noticed that for LiCdN, the DOS increases towards the  $p$ -region, whereas for all other compounds, it increases near the  $n$ -region.

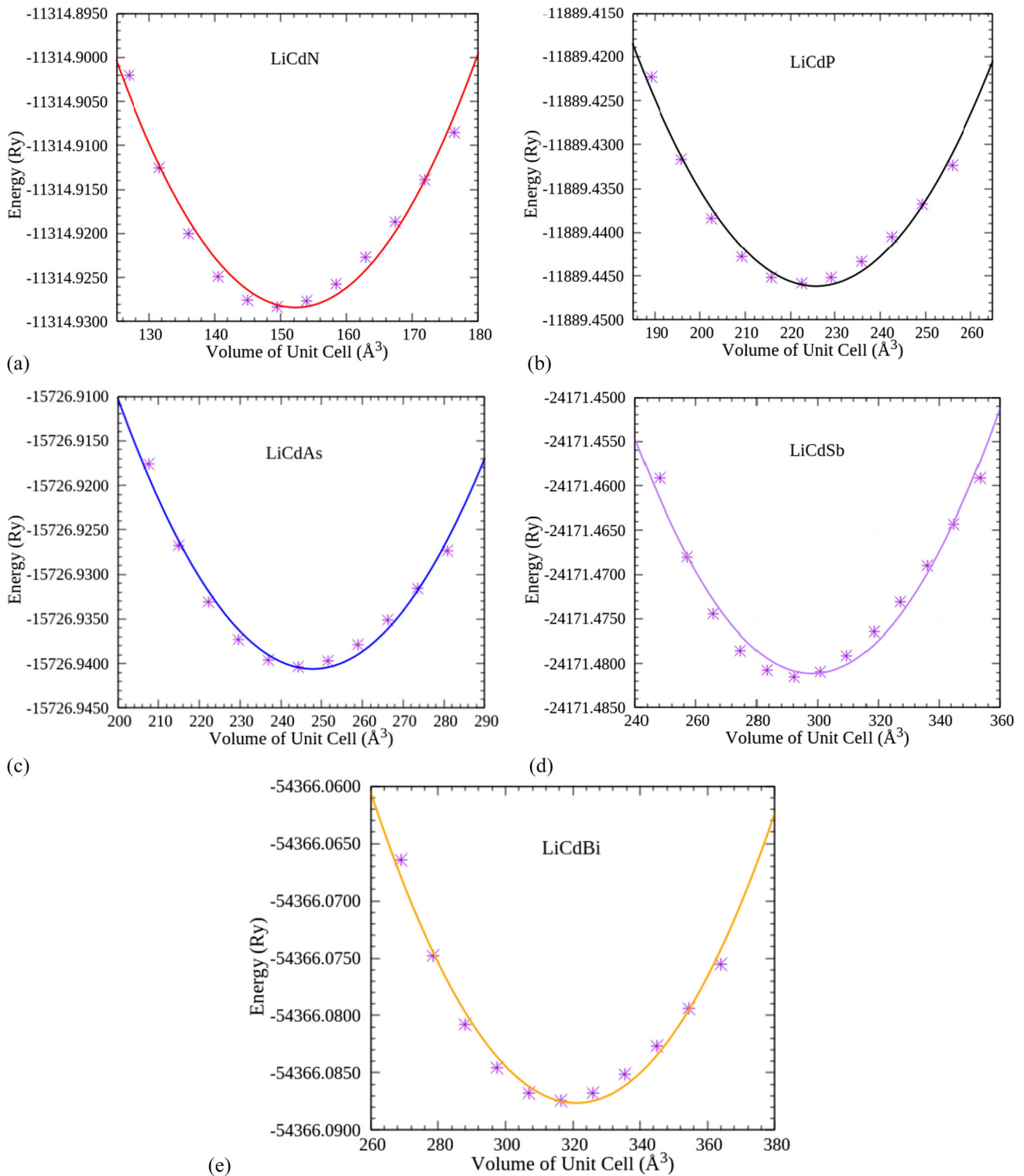


**Figure 1.** Variation in energy with the volume of LiCdX (X = N, P, As, Sb and Bi) half-Heusler compounds.

### 3.3 Optical properties

The optical parameters of a compound explain how electromagnetic (EM) radiation deals with it. The complex dielectric function gives a straightforward explanation

of these parameters. It specifies the photon–electron interaction in a material, and thus for a tiny wave vector, it specifies the system’s linear reaction to the incoming EM energy. Ehrenreich and Cohen’s equation state this complex quantity as follows [31]:

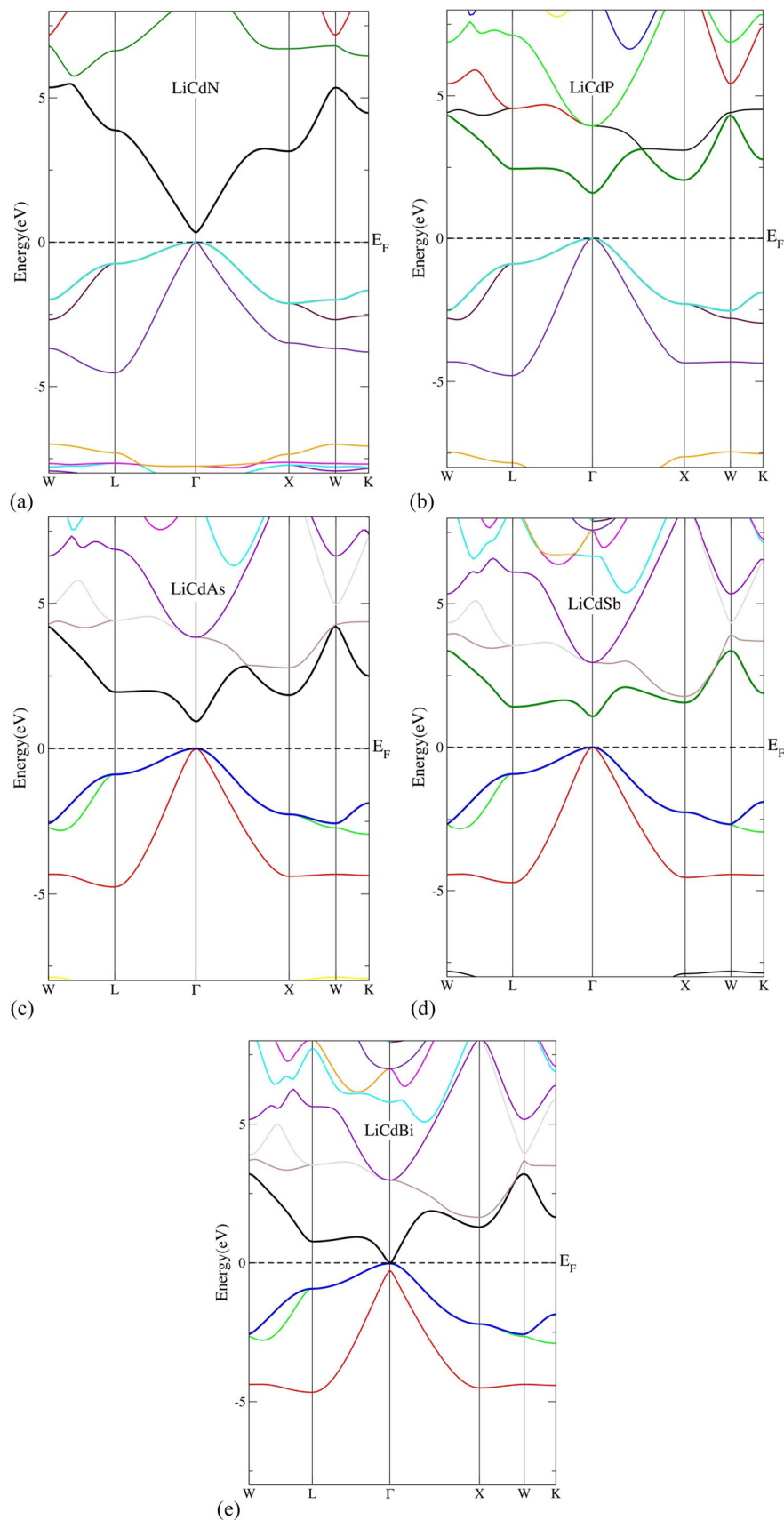


**Figure 2.** Electronic band structure plots of (a) LiCdN, (b) LiCdP, (c) LiCdAs, (d) LiCdSb and (e) LiCdBi half-Heusler compounds.



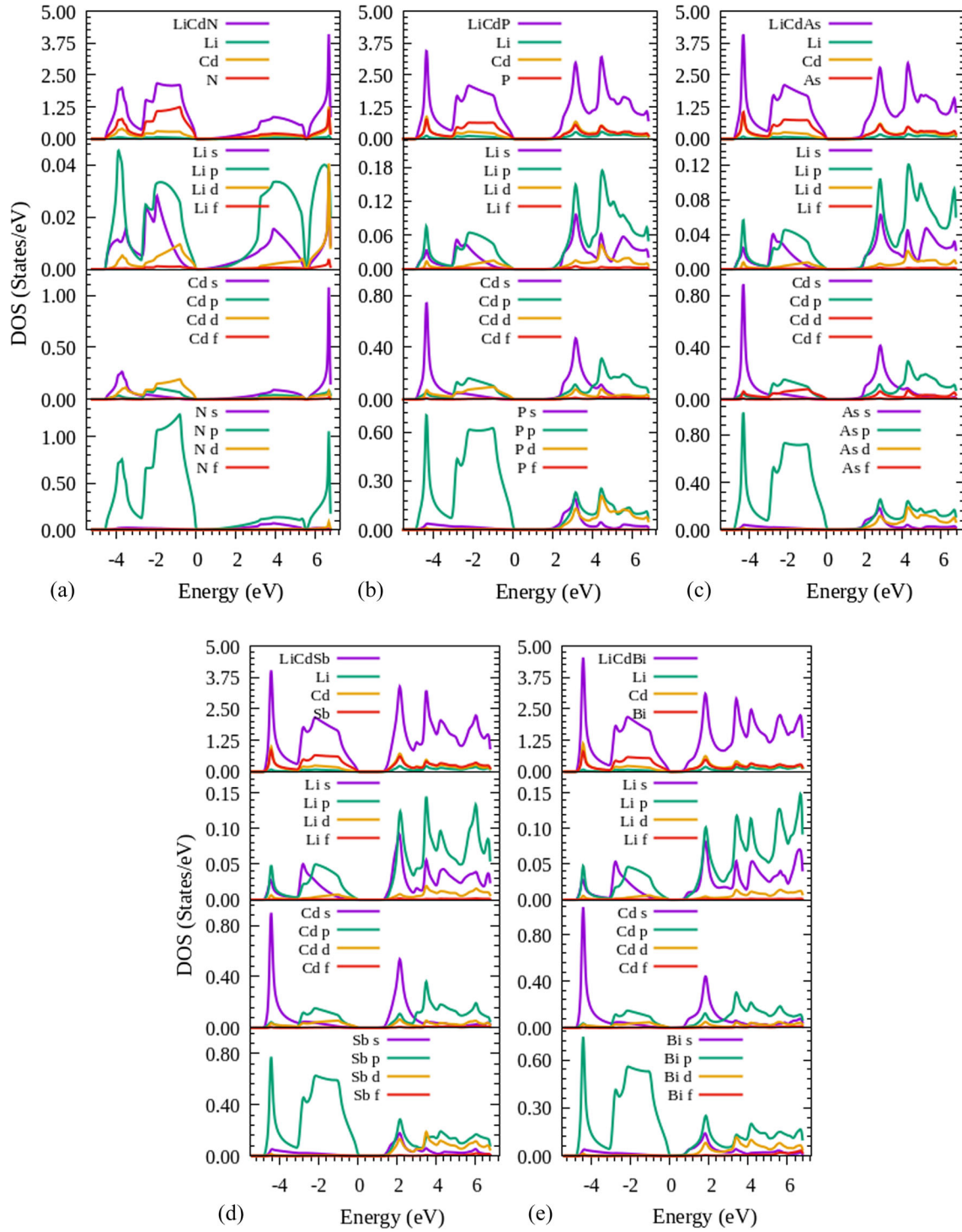


**Figure 3.** Total and partial DoS plots of (a) LiCdN, (b) LiCdP, (c) LiCdAs, (d) LiCdSb and (e) LiCdBi half-Heusler compounds.

$$\varepsilon(\omega) = \varepsilon_1(\omega) + i\varepsilon_2(\omega).$$

Here,  $\omega$  symbolises the angular frequency of EM energy received by the specimen. Electronic polarisation and anomalous dispersion are associated with

(1) the real component of the complex dielectric function  $\varepsilon_1(\omega)$  while its imaginary component  $\varepsilon_2(\omega)$  can be used to determine optical absorption. The dielectric function's imaginary component  $\varepsilon_2(\omega)$  is given as follows [32]:

$$\varepsilon_2(\omega) = \frac{4e^2\pi^2}{\omega^2 m^2} \sum_{i,j} \times \int |i|M|j|^2 f_i(1-f_i) X \delta(E_f - E_i - \hbar\omega) d^3k. \quad (2)$$

The dipole matrix is denoted by  $M$ , and the initial and final states (valence and conduction band, respectively) are denoted by  $i$  and  $j$ , respectively.  $f_i$  is the Fermi distribution function of the valence band,  $\delta(E_f - E_i - \hbar\omega)$  signifies the difference in energy between the conduction and valence bands at the  $k$ -point caused by the absorption of a photon of energy  $\hbar\omega$ . The electronic charge, the decreased Planck's constant ( $\hbar = h/2\pi$ ), the angular frequency of the incident photon and the mass of the electron are represented by  $e$ ,  $\hbar$ ,  $\omega$  and  $m$ , respectively. Using the Kramers–Kronig equation [33], the dielectric function's real component  $\varepsilon_1(\omega)$  can be determined as

$$\varepsilon_1(\omega) = 1 + \frac{2}{\pi} P \int_0^\infty \frac{\omega' \varepsilon_2(\omega')}{\omega'^2 - \omega^2} d\omega'. \quad (3)$$

The principal value of the integral is denoted by  $P$ . The dielectric function  $\varepsilon(\omega)$  was explored to study the response of the tested materials to incident radiation. Using  $\varepsilon_1(\omega)$  and  $\varepsilon_2(\omega)$ , the remaining optical characteristics, such as optical conductivity  $\sigma(\omega)$ , extinction coefficient  $k(\omega)$ , reflectivity  $R(\omega)$ , absorption coefficient  $\alpha(\omega)$ , refractive index  $n(\omega)$  and energy loss function  $E_{\text{loss}}(\omega)$  can be calculated [34].

$$\sigma(\omega) = \frac{\omega \varepsilon_2}{4\pi} \quad (4)$$

$$k(\omega) = \left[ \frac{\sqrt{[\varepsilon_1(\omega)]^2 + [\varepsilon_2(\omega)]^2}}{2} - \frac{\varepsilon_1(\omega)}{2} \right]^{1/2} \quad (5)$$

$$R(\omega) = \left| \frac{\sqrt{\varepsilon(\omega)} - 1}{\sqrt{\varepsilon(\omega)} + 1} \right|^2 \quad (6)$$

$$\alpha(\omega) = \sqrt{2}(\omega) \left( \sqrt{[\varepsilon_1(\omega)]^2 + [\varepsilon_2(\omega)]^2} - \varepsilon_1(\omega) \right)^{1/2} \quad (7)$$

$$n(\omega) = \left[ \frac{\sqrt{[\varepsilon_1(\omega)]^2 + [\varepsilon_2(\omega)]^2}}{2} + \frac{\varepsilon_1(\omega)}{2} \right]^{1/2} \quad (8)$$

and

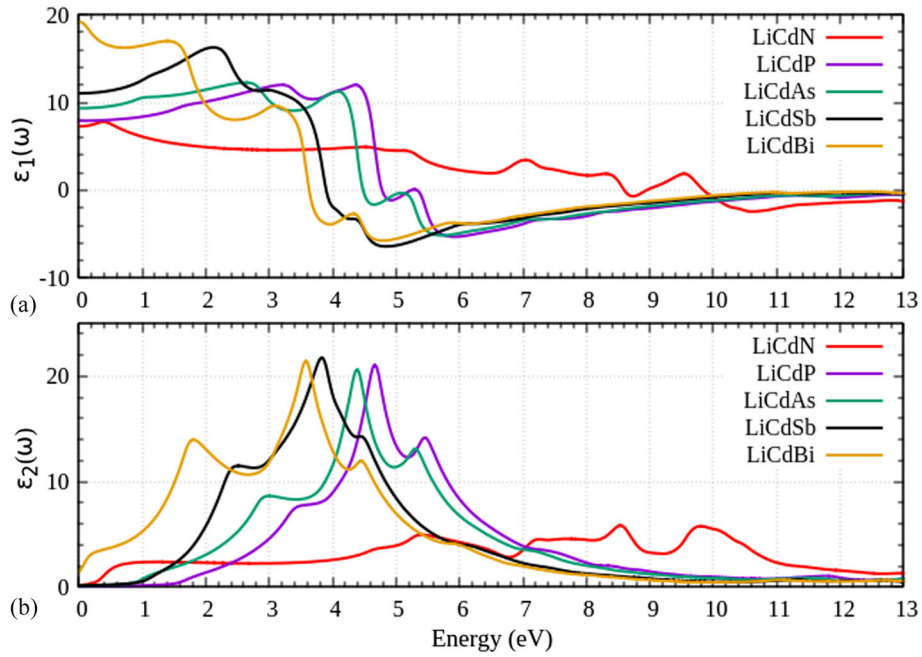
$$E_{\text{loss}}(\omega) = -\text{Im} \left( \frac{1}{\varepsilon} \right) = \frac{\varepsilon_2(\omega)}{[\varepsilon_1(\omega)]^2 + [\varepsilon_2(\omega)]^2}. \quad (9)$$

Figures 4–7 depict the expected optical properties for the stable configuration with incident EM radiation energies ranging up to 13 eV.

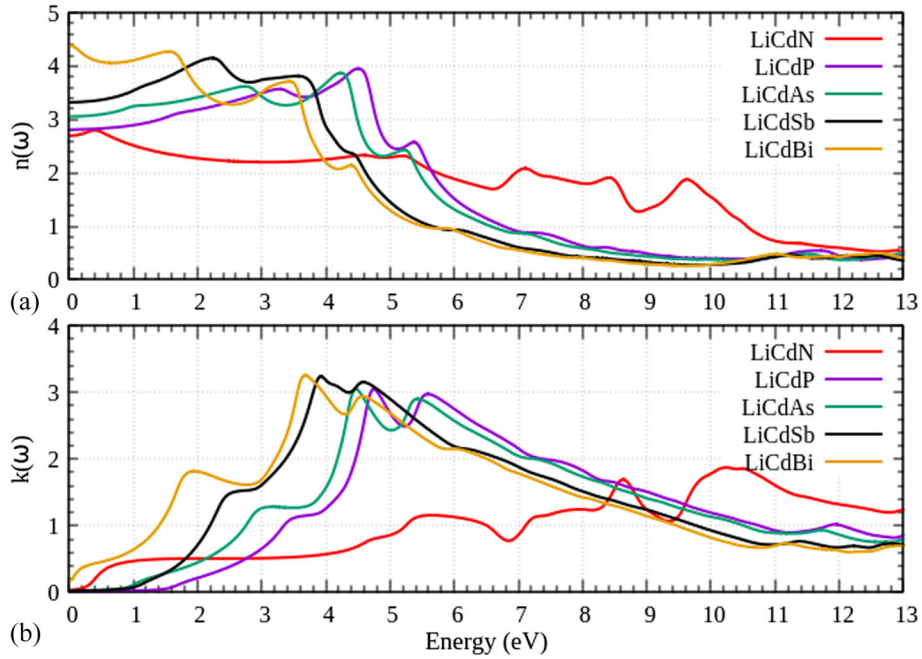
Figures 4a and 4b represent the variation in  $\varepsilon_1(\omega)$  and  $\varepsilon_2(\omega)$  with varying incident EM energy. The dielectric constant of a compound is indicated by the static value of  $\varepsilon_1(\omega)$ , i.e.  $\varepsilon_1(0)$ . Figure 4a shows that the values of  $\varepsilon_1(0)$  for the titled compounds are 7.275, 7.907, 9.339, 11.037 and 19.189, respectively. As a result, we have seen that the dielectric constants of these materials grow with the size of the X atom. The greater the value of  $\varepsilon_1(0)$ , the greater the reaction to incident EM radiation. The variation in  $\varepsilon_1(\omega)$  of various materials as a function of the incident EM energy is depicted in figure 4a. The value of  $\varepsilon_1(\omega)$  for these materials first grows slowly with increasing energy. Then, after reaching its ultimate value, it decreases with a number of ups and downs and turns out to be negative in the region of 3.65–13 eV and finally, tiny growth in the direction of zero is noted. The peaks of  $\varepsilon_1(\omega)$  are observed in the visible section for all the materials, indicating that these materials have the greatest response to the visible spectrum.

Figure 4b demonstrates the threshold energy values  $\varepsilon_2(\omega)$  for the studied materials that lie between 0 and 1.55 eV. These values denote the optical band gap of these compounds, which is very close to the computed electronic band gap. It demonstrates a high level of precision in the current results. For all the materials,  $\varepsilon_2(\omega)$  shows a fine maximum. Figures 5a and 5b show the refractive index  $n(\omega)$  and the extinction coefficient  $k(\omega)$ , respectively. For LiCdX (X = N, P, As, Sb and Bi), figure 5a shows the static refractive index ranging from 2.697 (for LiCdN) to 4.383 (LiCdBi), which upsurges along with the incident EM energy in the IR and visible sections. With increasing incident radiation energy, it begins to decline but never becomes negative, and the materials keep on transparent. The refractive index validates the explored isotropic behaviour of the materials, i.e., it remains directionally invariant. We discovered that the dielectric tensor  $\varepsilon(\omega)$  spectra in figure 4a abide by the refractive index  $n(\omega)$  spectra in figure 4a. The hindering in the amplitude of the oscillations of incident energy of the electric vector is associated with the extinction coefficient. The peak value of  $k(\omega)$  was discovered in figure 5b at the point where  $\varepsilon_1(\omega)$  is negligible. After achieving its maximum, it begins to drop as the energy of the incident radiation increases.

The conduction of photoelectrons in the vicinity of EM energy is used to describe optical conductivity  $\sigma(\omega)$ . Figure 6a shows the optical conductivity spectra for the incident energy. The optical conductivity of the titled compounds increases with the increasing frequency of EM energy until it reaches its optimum value in the UV region. The absorption coefficient of a compound shows how much of the incident radiation is soaked by a unit



**Figure 4.** Dielectric tensor spectra of LiCdX (X = N, P, As, Sb and Bi) half-Heusler compounds. (a) displays its real part  $\epsilon_1(\omega)$  and (b) displays its imaginary part  $\epsilon_2(\omega)$ .



**Figure 5.** (a) displays refractive index  $n(\omega)$  and (b) displays extinction coefficient  $k(\omega)$  of LiCdX (X = N, P, As, Sb and Bi) half-Heusler compounds.

depth of this compound. A greater absorption coefficient signifies that the material is more effective in moving electrons from their valance to conduction bands. Figure 6b exhibits the relationship between the energy of incident radiation and the deviation in the absorption coefficient  $\alpha(\omega)$  of LiCdX (X = N, P, As, Sb and Bi). In

a similar area, where optical conductivity appears to be zero, absorption is almost negligible, as shown in this diagram. It has also been noticed that when absorption is at its highest, optical conductivity is also at its highest, confirming the theoretical concept and thus the accuracy of the projected outcomes.



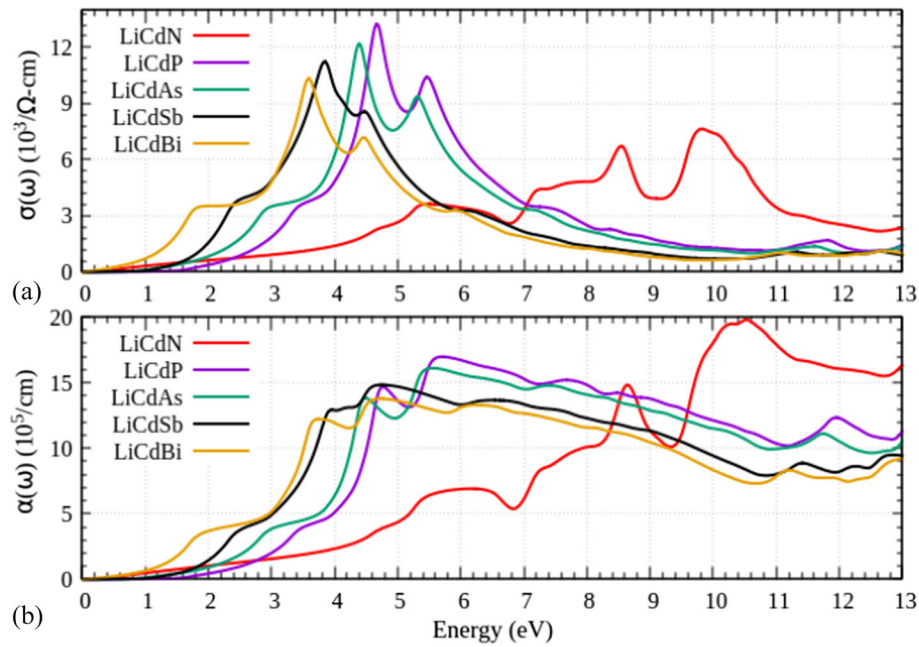


**Figure 6.** (a) displays optical conductivity  $\sigma(\omega)$  and (b) displays absorption coefficient  $\alpha(\omega)$  of LiCdX (X = N, P, As, Sb and Bi) half-Heusler compounds.

Figure 7a demonstrates the optical reflectivity  $R(\omega)$  and from this figure, it has been concluded that the static value of reflectivity  $R(0)$  of LiCdX (X = N, P, As, Sb and Bi) is 21.1%, 22.6%, 25.7%, 28.9% and 39.5%, respectively. The maximum reflectivity has been recorded for LiCdBi, which reaches 61.8% in the UV region. Because of this, the investigated materials are also efficient in the near-infrared and visible spectra and can function as UV shields. The energy loss function  $E_{\text{loss}}(\omega)$  for electrons is shown in figure 7b. It depicts the energy loss of a fast-moving electron inside a specimen. The maximum values of  $E_{\text{loss}}(\omega)$  are related to plasma resonance (coupled oscillations of valence electrons) and plasma frequency ( $\omega_p$ ) (the frequency at which plasma resonance occurs). The UV region yields the pronounced  $E_{\text{loss}}(\omega)$  peaks of the chosen materials (beyond 7.0 eV). Table 1 shows the calculated static values of numerous optical properties including the dielectric constant  $\epsilon_1(0)$ , reflectivity  $R(0)$  and refractive index  $n(0)$  as well as a comparison with other available values.

Figures 4–7 show that the optical spectra of LiCdN show different behaviour compared to the optical spectra of the LiCdP, LiCdAs, LiCdSb and LiCdBi compounds. Its reason may be understood with the help of the band structure and DOS of these materials. The optical spectra are very much related to the absorption and energy loss of the incident EM radiation. It is quite clear from the band structure and DOS of these materials that in LiCdN the number of bands near the conduction band minima is quite less than the other

investigated materials. Therefore, in LiCdN, for a wide range of incident EM energy, a smaller number of transitions take place, which consequently shows a lesser number of peaks in comparison to other considered materials. DOS of LiCdN confirms that the contribution of the Cd atom in the electronic transition in this material is quite low in comparison to the other investigated materials which again confirms the reason behind a smaller number of electronic transitions in it.

### 3.4 Thermoelectric properties

The figure of merit of a compound can be defined using  $ZT = S^2\sigma T/\kappa$  and used to determine their efficiency.  $S^2\sigma$  is identified as the power factor (PF), where  $S$  is the thermopower or Seebeck coefficient,  $\sigma$  is the electrical conductivity,  $\kappa$  ( $= \kappa_e + \kappa_l$ ) is the total electron and phonon contributions in thermal conductivity and  $T$  is the absolute temperature. A constant relaxation time method was utilised to compute transport parameters using the BoltzTraP algorithm [35]. The Seebeck coefficient ( $S$ ) can be calculated autonomously of any adaptable limitations (i.e.,  $S$  does not depend on the relaxation time or any other limitation in the materials) in this constant relaxation time approach (CRTA), but  $\kappa_e$  and  $\sigma$  must be calculated per unit relaxation time. As a result, rather than measuring the definite power factor  $S^2\sigma$ , the power factor per unit relaxation time ( $S^2\sigma/\tau$ ) had been calculated. All the transport criteria have been calculated for chemical potential and variation in these parameters has been represented graphically in figure 8.

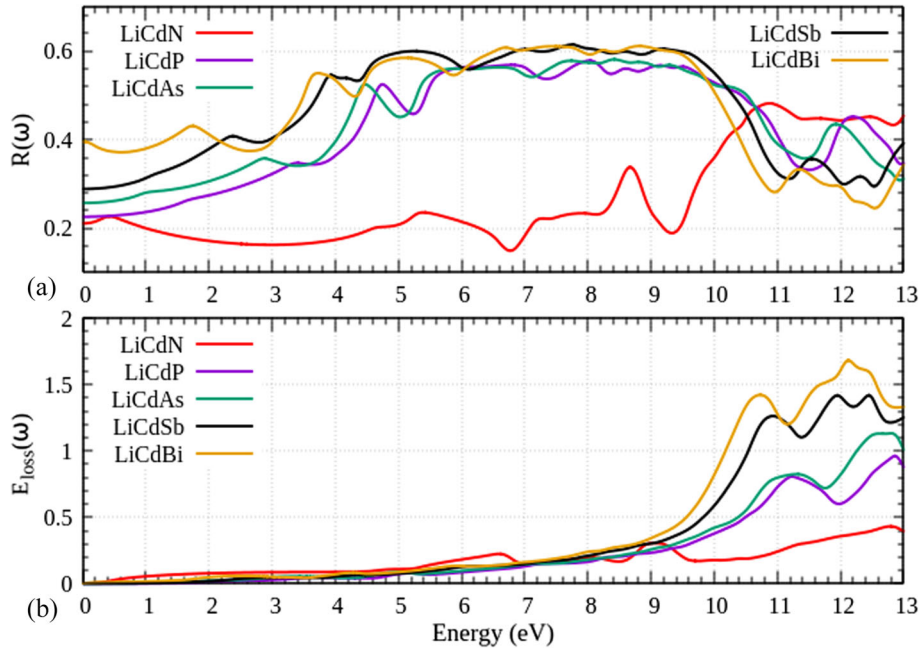


**Figure 7.** (a) displays reflectivity  $R(\omega)$  and (b) displays energy loss function  $E_{\text{loss}}(\omega)$  of  $\text{LiCdX}$  ( $X = \text{N, P, As, Sb and Bi}$ ) half-Heusler compounds.

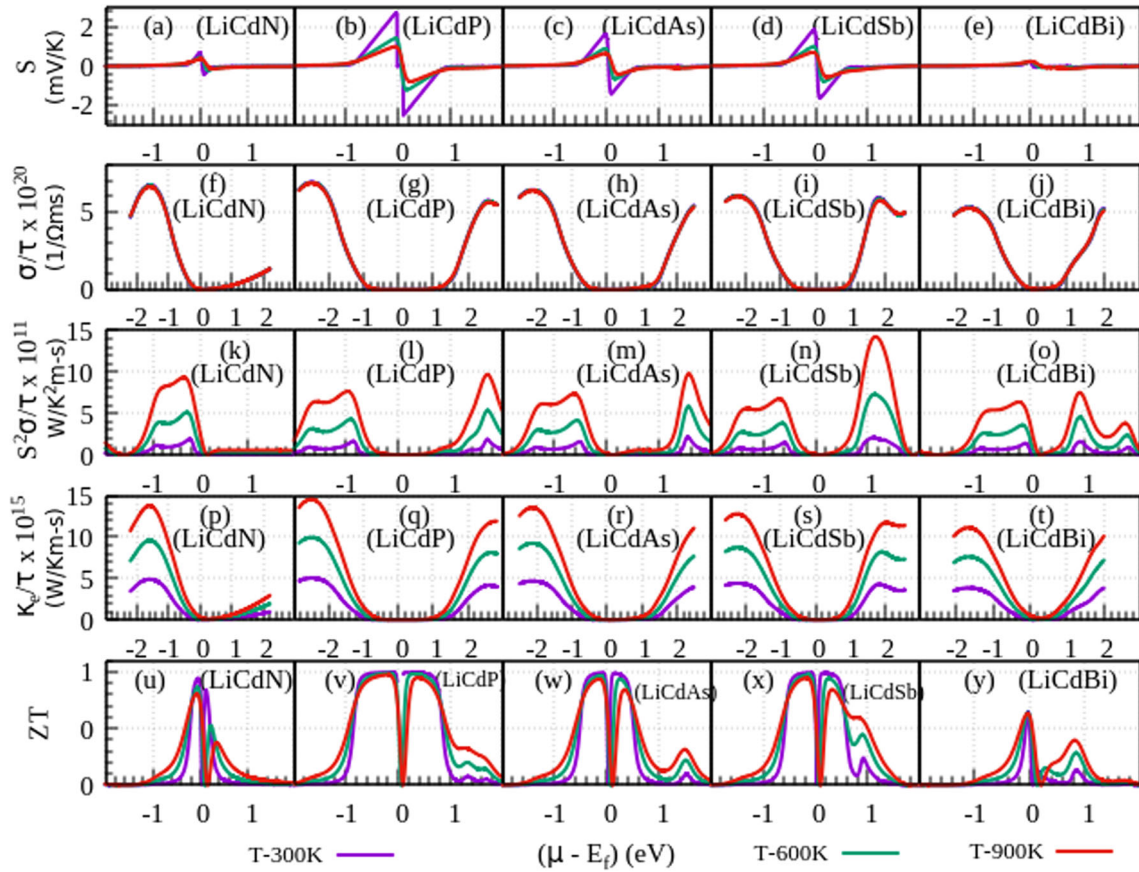


**Figure 8.** Thermoelectric parameters of  $\text{LiCdX}$  ( $X = \text{N, P, As, Sb and Bi}$ ) half-Heusler compounds for chemical potential at 300, 600 and 900 K.

The analysis of thermoelectric parameters is insufficient without a discourse on the optimal doping level. Various thermoelectric parameters are relatively simple to explain concerning the chemical potential, but experimental scientists examine these characteristics concerning doping levels or charge carriers. Hence, a variation in these parameters with carrier concentration has also been represented graphically in figure 9.

The Seebeck coefficient is a crucial component that reflects the nature of a specimen's dominant charge carriers and is linked with its band structure. Its affirmative and negative values indicate *p*- and *n*-type doping in the compound, respectively. For diverse chemical potential ( $\mu - E_f$ ), the Seebeck coefficient has been determined and doping concentrations at different temperatures and displayed in figures 8a–8e and 9a–9e, respectively. We can see from these graphs that *S* has two maxima, one for the *p*-region and the other for the *n*-region. LiCdBi has the lowest *S* values of all of these materials because it has a narrow range of energy. For the explored materials, the *S* significantly reduces as temperature increases, indicating that, it will behave like a decay factor for thermoelectric efficiency at high temperatures. The computed

maximum values of *S* of the compounds in the *p*- and *n*-regions at 300 and 900 K are shown in table 2. From these figures and tabularised data, it may be concluded that the in the *p*-region (just below the Fermi level) and close to the band-gap's middle (i.e. for low optimum carrier concentrations), *S* is greater. These minima and maxima can be obtained with very low doping concentrations because they lie within a very constrained range of the chemical potential. Aside from this range, *S* quickly decreases for higher doping concentrations.

In figures 8f–8j and 9f–9j, we have presented electrical conductivity ( $\sigma/\tau$ ) for chemical potential ( $\mu - E_f$ ) and carrier concentration (carrier/u.c.), respectively at diverse temperatures. In contrast to *S* values, values of  $\sigma/\tau$  act consistently throughout all temperature ranges. Figures display that the value of  $\sigma/\tau$  for the overall range of  $\mu - E_f$  and doping concentrations is higher for the *p*-type configuration of the studied compounds; while in the proximity of the middle of the band gap of these materials (except LiCdN), i.e., for optimal carrier concentrations,  $\sigma/\tau$  is stronger in *n*-region; however, for LiCdN it is stronger in *p*-region. This behaviour of LiCdN can be understood with the help of its DOS plot

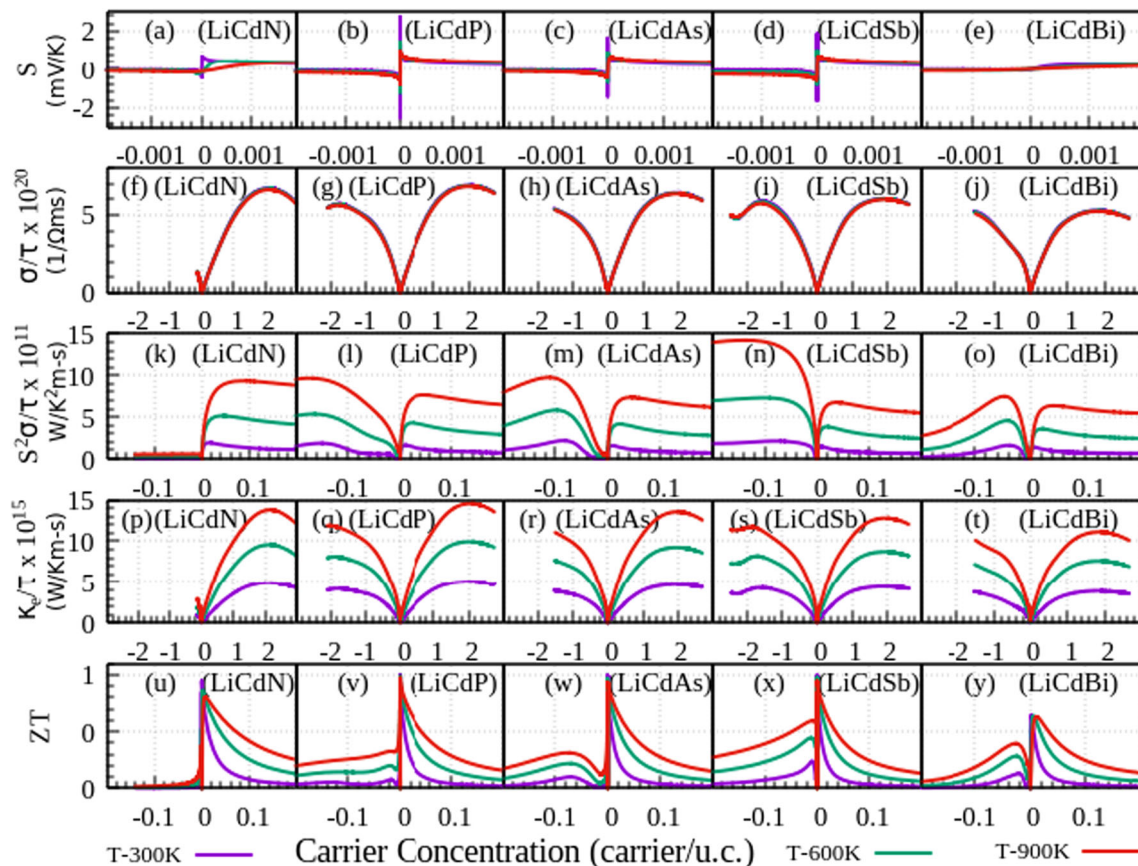


**Figure 9.** Thermoelectric parameters of LiCdX (X = N, P, As, Sb and Bi) half-Heusler compounds for career concentration at 300, 600 and 900 K.

**Table 2.** Thermoelectric parameters: Seebeck coefficient ( $S$ ); electrical conductivity per unit relaxation time ( $\sigma/\tau$ ), power factor per unit relaxation time ( $S^2\sigma/\tau$ ), electronic thermal conductivity per unit relaxation time ( $\kappa_e/\tau$ ), optimal carrier concentration per unit cell for maximum PF ( $N$ ) and figure of merit ( $ZT = S^2\sigma T/\kappa_{\text{total}}$ ).

Compounds	$S$ (mV/K)			$\sigma/\tau$ ( $10^{20}/\Omega\text{ms}$ )			PF ( $10^{11}\text{ W/K}^2\text{ m s}$ )			$\kappa/\tau$ ( $10^{15}\text{ W/K m s}$ )			$N$ (carriers/u.c.)			ZT		
	300 K	900 K		300 K	900 K		300 K	900 K		300 K	900 K		300 K	900 K		300 K	900 K	
LiCdN																		
p-type	0.69	0.36		0.11	0.54		1.89, 1.92 <sup>a</sup>	9.34		0.12	1.85		0.015, 0.016 <sup>a</sup>	0.086		0.94	0.81	
n-type	−0.43	−0.14		0.01	0.08		0.09	0.56		0.01	0.22		−0.0001	−0.002		0.84	0.38	
LiCdP																		
p-type	2.73	0.99		0.08	0.41		1.62, 1.67 <sup>a</sup>	7.65		0.10	1.43		0.008, 0.008 <sup>a</sup>	0.047		1.00	0.97	
n-type	−2.52	−0.80		1.38	1.55		1.84	9.66		1.06	4.02		−0.148	−0.175		1.00	0.95	
LiCdAs																		
p-type	1.64	0.64		0.08	0.40		1.56, 1.61 <sup>a</sup>	7.36		0.10	1.38		0.008, 0.009 <sup>a</sup>	0.045		0.99	0.94	
n-type	−1.41	−0.42		0.88	1.11		2.15	9.76		0.69	3.09		−0.085	−0.114		0.99	0.84	
LiCdSb																		
p-type	1.86	0.70		0.08	0.35		1.46, 1.50 <sup>a</sup>	6.75		0.09	1.24		0.007, 0.008 <sup>a</sup>	0.037		0.99	0.95	
n-type	−1.64	−0.57		0.90	1.30		2.10	14.23		0.71	3.82		−0.078	−0.140		0.99	0.84	
LiCdBi																		
p-type	0.23	0.22		0.08	0.37		1.36	6.35		0.09	1.27		0.007	0.041		0.64	0.63	
n-type	−0.06	−0.14		0.61	0.65		1.58	7.48		0.48	1.91		−0.041	−0.047		0.13	0.40	

<sup>a</sup>Ref [21]



(figure 3a). From figure 3a, the electron concentration near CBM is remarkably low, and a lesser number of electrons actively engage in current conduction, resulting in a low value of  $\sigma/\tau$  of LiCdN in the  $n$ -region. From figure 8f–8j, it is clear that as  $\mu - E_f$  increases,  $\sigma/\tau$  increases. Since the upsurge in  $\mu - E_f$  improves charge carrier mobility,  $\sigma/\tau$  improves. As a result, we find that, contrary to the  $S$  trend, these compounds are better in the  $n$ -region than in the  $p$ -region for optimal carrier concentrations. Moreover, we must contend with very low  $\sigma/\tau$  values to achieve optimal doping concentrations. Additionally, to attain the best doping concentrations, we must contend with extremely low  $\sigma/\tau$  values. Table 2 shows the values of  $\sigma/\tau$  that correspond to the highest power factor at 300 and 900 K.

We have calculated the PF in terms of the relaxation time ( $S^2\sigma/\tau$ ), using the aforementioned thermoelectric characteristics. Figures 8k–8o illustrate the deviation in PF with chemical potential ( $\mu - E_f$ ) whereas figure 9k–9o show the variation in PF for doping concentration. When ( $\mu - E_f$ ) is in the vicinity of the middle of the energy band gap, the PF can be as low as possible because  $S$  is virtually zero there and  $\sigma/\tau$  is negligible because of the low carrier concentration. Furthermore, as ( $\mu - E_f$ ) increases, both  $\sigma/\tau$  and  $S$  increase with it. In contrast to the quick decrease in  $S$  that occurs with an increase in  $\mu - E_f$ , the value of  $\sigma/\tau$  continues to rise. As a result, two distinct peaks are formed in these compounds, for the  $p$ - and  $n$ -regions, respectively. The highest PF for both  $p$ - and  $n$ -regions of LiCdSb is observed at around 900 K, and this steadily drops as temperature drops. The values of PF of the  $p$ - and  $n$ -regions at 300 and 900 K are shown in table 2. According to this analysis, there is a small window of carrier concentrations when PF reigns supreme. At 300 and 900 K, the ideal carrier concentration to generate the maximum PF has been represented in this table. The proposed optimal carrier concentration offers a small window for experimental experts to fabricate high-thermoelectric-efficiency materials. The electronic thermal conductivity ( $\kappa_e/\tau$ ) has been determined at three different temperatures for the chemical potential ( $\mu - E_f$ ) and carrier concentration (carrier/u.c.) and these results have been presented in figures 8p–8t and 9p–9t, respectively. To attain supreme thermoelectric efficiency,  $\kappa_e/\tau$  needs to be the lowest. From these figures, it has been observed that  $\kappa_e$  rises with rising temperatures. Thus, the lowest value of  $\kappa_e/\tau$  can be obtained at 300 K. From these figures, we have found that  $\kappa_e/\tau$  is the lowest in the regions where  $S$  is maximum. Hence, in these regions, the explored materials have maximum

efficiency. With varying chemical potential,  $\kappa_e/\tau$  follows the same pattern as  $\sigma/\tau$ , that is, it rises with growing chemical potential values though by a lesser fraction than  $\sigma/\tau$ . In contrast to  $\sigma/\tau$ , for a specific chemical potential value,  $\kappa_e/\tau$  has different values at different temperatures. Figures 8p–8t and 9p–9t demonstrate that  $\kappa_e/\tau$  is greater in the  $p$ -region than in the  $n$ -region. Like  $\sigma/\tau$ , it shows that the  $n$ -region has a bigger value of  $\kappa_e/\tau$  than the  $p$ -region for small carrier concentrations. At 300 and 900 K, corresponding to the maximum PF and optimal doping concentrations, the highest value of  $\kappa_e/\tau$  for both regions is shown in table 2.

The figure of merit of the investigated half-Heuslers at 300, 600 and 900 K has been calculated based on the previously mentioned transport factors. The variance in ZT is shown in figures 8u–8y and 9u–9y with chemical potential and carrier concentrations respectively. For achieving the higher ZT, thermal conductivity must be lower and PF must be higher. Reaching greater values of ZT remains difficult because of the discrepancies between  $S$ ,  $\sigma$  and  $\kappa$ , even though no theoretical upper limit is established to achieve the highest value of ZT. As a result, to raise the ZT, there must be an agreement among such disparate factors. The efficiency of thermoelectric substances is represented by ZT. From figure 8u–8y, we have observed that at 300 K LiCdN and LiCdBi demonstrate greater ZT for the  $p$ -region than the  $n$ -region, and the remaining materials exhibit almost equal values of ZT in both regions, while at 900 K all the compounds show higher ZT in the  $p$ -region. Figures 9u–9y validate the result of figures 8u–8y, at very minimal doping concentrations, and experimental experts are motivated to work on these compounds. It is evident from the figures that as the temperature rises, except for  $n$ -type LiCdBi, ZT of all the half-Heuslers decreases, which validates that these materials are best at lower temperatures.  $n$ -type LiCdBi exhibits higher ZT at higher temperatures, i.e., good thermoelectric performance at higher temperatures. For  $p$ - and  $n$ -regions, at 300 and 900 K, the largest value of ZT are given in table 2. We see that among all the explored compounds, LiCdP exhibits the maximum ZT ( $ZT = 1$ ) in both the regions at room temperature and for LiCdAs and LiCdSb it reaches unity, while LiCdN and LiCdBi show lesser performance among all the investigated materials. A material with a larger ZT is expected to have a higher efficiency for the conversion of heat into electricity [36]. Previous researchers [37–44] found that  $n$ -type ZrNiSn and  $p$ -type ZrCoSb-based HH alloys show a maximum ZT of  $\sim 1.0$  and  $\leq 0.8$ , respectively. Hence LiCdP, LiCdAs and LiCdSb demonstrate great potential for thermoelectric applications.

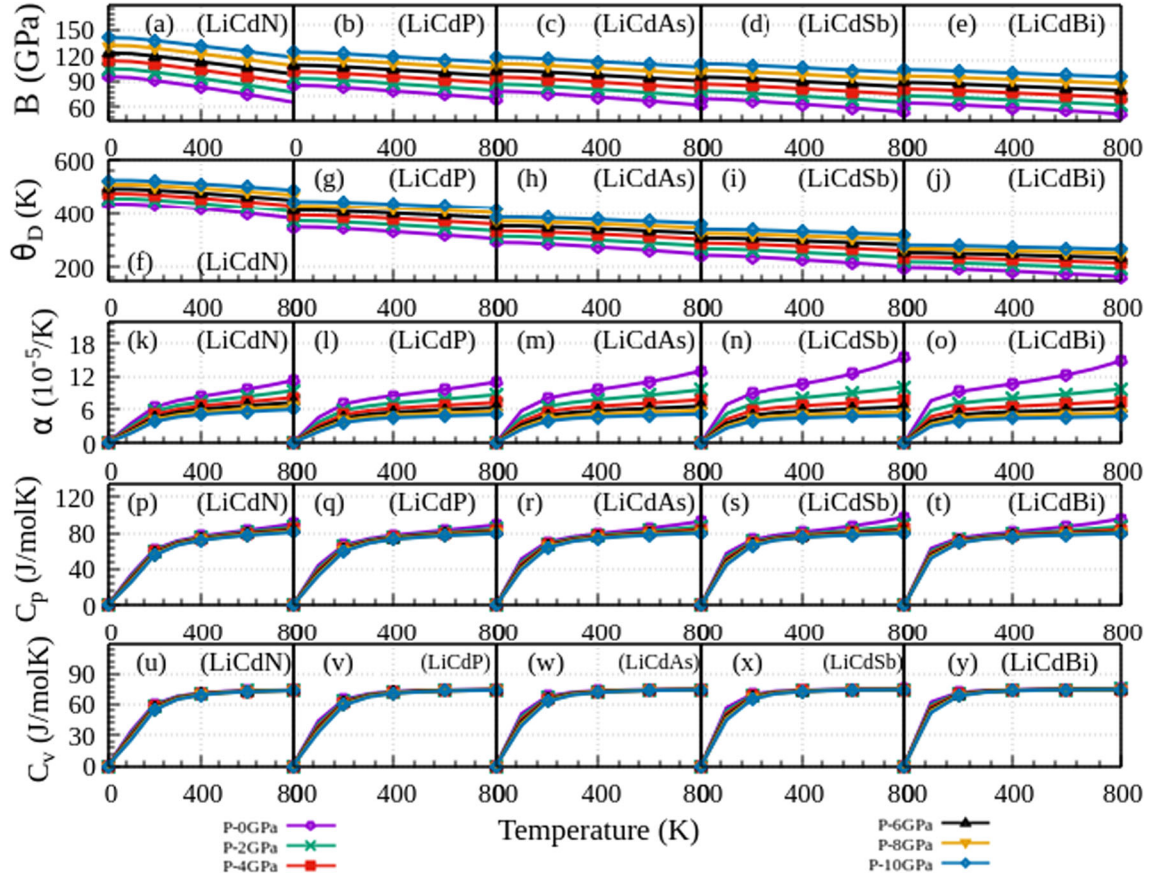


**Figure 10.** Thermodynamic parameters of LiCdX (X = N, P, As, Sb and Bi) half-Heusler compounds with the temperature at continual pressure from 0–10 GPa.

### 3.5 Thermodynamic properties

We estimated the thermodynamic parameters of the titled compounds using the Gibbs2 programme [45]. We used the total energy as a function of volume  $E(V)$  for several primitive cells in conventional thermodynamic calculations to determine the thermodynamic properties for varying temperature and pressure ranges [46,47]. Using the quasiharmonic model, the thermodynamic characteristics of the studied compounds were computed in the temperature range from 0 to 800 K, and the effects of pressure were looked at from 0 to 10 GPa. The variance of bulk modulus with temperature and pressure is shown in figures 10a–10e. It is interesting to note that at a particular pressure, the bulk modulus marginally decreases with increasing temperature, while at a particular temperature, it greatly increases with increasing pressure. In the quasiharmonic Debye model, the acoustic Debye temperature is a crucial parameter [48]. Figures 10f–10j illustrate the variation in acoustic Debye temperature  $\Theta_D$  with respect to

temperature. The graph suggests that pressure and temperature have a reverse effect on  $\Theta_D$ . This implies that pressure and temperature have an impact on how frequently atoms vibrate in the investigated materials.

Figures 10k–10o display the variation in the thermal expansion coefficient with temperature for the pressure range 0–10 GPa. According to the graph, it rises quickly in the temperature range of 0–200 K, then gradually increases. Above 300 K, particularly at high pressures, it grows roughly linearly with a mild slope. A crucial factor that offers a thorough understanding of the vibrational characteristics of the materials for several uses is their heat capacity. Figures 10p–10t and 10u–10y demonstrate the change in heat capacity ( $C_p$  and  $C_v$ ) for changing temperatures, respectively. It can be interpreted that heat capacity ( $C_p$  and  $C_v$ ) obey the  $T^3$  law at low temperatures, while at high temperatures,  $C_p$  grows with temperature, and due to suppression of an anharmonic consequence  $C_v$  becomes constant. The value at which  $C_v$  becomes constant is referred to as the Dulong–Petit limit.

#### 4. Summary and conclusions

The first-principles analysis was used to investigate the fundamental physical properties of LiCdX (where X = N, P, As, Sb and Bi) half-Heusler materials. The filled tetrahedral structure of these materials shows semi-conducting behaviour (except LiCdBi) with directivity at  $\Gamma$ – $\Gamma$ , whereas LiCdBi shows metallic nature. The obtained results match experimental and theoretical data very well. In the near-infrared and visible ranges, these are good photovoltaics, but far-infrared and ultraviolet light is restricted. By examining thermoelectric characteristics, it has been discovered that the PF of these materials is larger in the  $n$ -region than in the  $p$ -region at optimal doping, while for a higher range of chemical potential, it is higher in the  $p$ -region. At 300 K, for LiCdP, LiCdAs and LiCdSb, ZT has a supreme value of 1.0, 0.99 and 0.99, respectively in both  $p$ - and  $n$ -regions, which affirms their potential thermoelectric materials in the  $p$ -region at room temperature. The studied thermodynamic properties have confirmed that these materials are thermodynamically stable. The results of this study will inspire experimental experts who will deal with these materials in the future.

#### References

- [1] M Singh, R Kumar, S Srivastava and T Kumar, *Phys. B: Condens. Matter* **640**, 414056 (2022)
- [2] Z A A R Almaghbash, O Arbouche, A Dahani, A Cherifi, M Belabbas, A Zenati, H Mebarki and A Hussain, *Int. J. Thermophys.* **42**, 1 (2021)
- [3] B Anissa, D Radouan and I K Durukan, *Opt. Quantum Electron.* **54**, 1 (2022)
- [4] A Azouaoui, A Hourmatallah, N Benzakour and K Bouslykhane, *J. Solid State Chem.* **310**, 123020 (2022)
- [5] H Nowotny and K Bachmayer, *Monatshefte für Chemie und verwandte Teile anderer Wissenschaften* **81**, 488 (1950)
- [6] H C Kandpal, C Felser and R Seshadri, *J. Phys. D* **39**, 776 (2006)
- [7] H Mehnane, B Bekkouche, S Kacimi, A Hallouche, M Djermouni and A Zaoui, *Superlatt. Microstruct.* **51**, 772 (2012)
- [8] S Curtarolo, G L Hart, M B Nardelli, N Mingo, S Sanvito and O Levy, *Nat. Mater.* **12**, 191 (2013)
- [9] S Ögüt and K M Rabe, *Phys. Rev. B* **51**, 10443 (1995)
- [10] D Kieven, R Klenk, S Naghavi, C Felser and T Gruhn, *Phys. Rev. B* **81**, 075208 (2010)
- [11] T Gruhn, *Phys. Rev. B* **82**, 125210 (2010)
- [12] F Casper, R Seshadri and C Felser, *Phys. Status Solidi A* **206**, 1090 (2009)
- [13] A Roy, J W Bennett, K M Rabe and D Vanderbilt, *Phys. Rev. Lett.* **109**, 037602 (2012)
- [14] P K Kamlesh, R Gautam, S Kumari and A S Verma, *Phys. B: Condens. Matter* **615**, 412536 (2021)
- [15] B Rani, A F Wani, S A Khandy, U B Sharopov, L Patra, K Kaur and S Dhiman, *Solid State Commun.* **351**, 114796 (2022)
- [16] F Casper, T Graf, S Chadov, B Balke and C Fels, *Semicond. Sci. Technol.* **27**, 063001 (2012)
- [17] S A Khandy, K Kaur, S Dhiman, J Singh and V Kumar, *Comput. Mater. Sci.* **188**, 110232 (2021)
- [18] H Bouafia, B Sahli, M Bousmaha, B Djebour, A Dorbane, S Mokrane and S Hiadsi, *Solid State Sci.* **118**, 106677 (2021)
- [19] X Ye, Z Feng, Y Zhang, G Zhao and D J Singh, *Phys. Rev. B* **105**, 104309 (2022)
- [20] M Sarwan, V A Shukoor and S Singh, in *Mathematics in computational science and engineering* edited by R Bhardwaj, J Mishra, S Narayan, G Suseendran (Wiley Online Library 2022) pp. 181–197
- [21] M K Yadav and B Sanyal, *J. Alloys Compd.* **622**, 388 (2015)
- [22] A Mellouki, L Kalarasse, B Bennecer and F Kalarasse, *Comput. Mater. Sci.* **42**, 579 (2008)
- [23] A Bouhemadou, S Bin-Omran, D Allali, S M Al-Otaibi, R Khenata, Y Al-Douri, M Chegaar and A H Reshak, *Mater. Res. Bull.* **64**, 337 (2015)
- [24] F Kalarasse, B Bennecer, A Mellouki and L Kalarasse, *Comput. Mater. Sci.* **43**, 791 (2008)
- [25] A Mellouki, L Kalarasse, B Bennecer and F Kalarasse, *Comput. Mater. Sci.* **44**, 876 (2009)
- [26] Z Wu and R E Cohen, *Phys. Rev. B* **73**, 235116 (2006)
- [27] J P Perdew, K Burke and M Ernzerhof, *Phys. Rev. Lett.* **77**, 3865 (1996)
- [28] F Tran and P Blaha, *Phys. Rev. Lett.* **102**, 226401 (2009)
- [29] P K Kamlesh, R Agarwal, U Rani and A S Verma, *Phys. Scr.* **96**, 115802 (2021)
- [30] U Rani, Y Soni, P K Kamlesh, A Shukla and A S Verma, *Int. J. Energy Res.* **45**, 13442 (2021)
- [31] U Rani, P K Kamlesh, R Agarwal, J Kumari and A S Verma, *Int. J. Quantum Chem.* **121**, e26759 (2021)
- [32] U Rani, P K Kamlesh, A Shukla and A S Verma, *J. Solid State Chem.* **300**, 122246 (2021)
- [33] P K Kamlesh, R Agrawal, U Rani and A S Verma, *Mater. Chem. Phys.* **275**, 125233 (2022)
- [34] P K Kamlesh, Pravesh, S Kumari and A S Verma, *Phys. Scr.* **95**, 095806 (2020)
- [35] G K H Madsen and D J Singh, *Comput. Phys. Commun.* **175**, 67 (2006)
- [36] R J Quinn and J-WG Bos, *Mater. Adv.* **2**, 6246 (2021)
- [37] C Fu, S Bai, Y Liu, Y Tang, L Chen, X Zhao and T Zhu, *Nature Commun.* **6**, 8144 (2015)
- [38] C Yu, T J Zhu, R Z Shi, Y Zhang, X B Zhao and J He, *Acta Mater.* **57**, 2757 (2009)
- [39] M Schwall and B Balke, *Phys. Chem. Chem. Phys.* **15**, 1868 (2013)
- [40] S Chen, K C Lukas, W Liu, C P Opeil, G Chen and Z Ren, *Adv. Energy Mater.* **3**, 1210 (2013)

- [41] W Xie, A Weidenkaff, X Tang, Q Zhang, J Poon and T M Tritt, *Nanomaterials* **2**, 379 (2012)
- [42] N S Chauhan, S Bathula, A Vishwakarma, R Bhardwaj, K K Johari, B Gahtori and A Dhar, *J. Materiomics* **5**, 94 (2019)
- [43] R He, H S Kim, Y Lan, D Wang, S Chen and Z Ren, *RSC Adv.* **4**, 64711 (2014)
- [44] X Yan, G Joshi, W Liu, Y Lan, H Wang, S Lee, J Simonson, S Poon, T Tritt and G Chen, *Nano Lett.* **11**, 556 (2010)
- [45] A Otero-de-la-Roza, D Abbasi-Pérez and V Luaña, *Comput. Phys. Commun.* **182**, 2232 (2011)
- [46] P Verma, C Singh, P K Kamlesh, K Kaur and A S Verma, *J. Mol. Model.* **29**, 23 (2023)
- [47] U Rani, P K Kamlesh, R Agrawal, A Shukla and A S Verma, *Energy Technol.* **10**, 2200002 (2022)
- [48] X Peng, L Xing and Z Fang, *Phys. B: Condens. Matter* **394**, 111 (2007)
- [49] R Bacewicz and T F Ciszczek, *Mater. Res. Bull.* **23**, 1247 (1988)
- [50] A Bouhemadou, *Mater. Sci. Semicond. Process.* **12**, 198 (2009)
- [51] R Bacewicz and T F Ciszczek, *Appl. Phys. Lett.* **52**, 1150 (1988)